

Anomalous Radio-Wave Scattering from Interstellar Plasma Structures

J. M. Cordes

Astronomy Department and NAIC, Cornell University; cordes@spacenet.tn.cornell.edu

T. Joseph W. Lazio

Code 7213, Naval Research Laboratory, Washington, DC 20375-5351; lazio@rsd.nrl.navy.mil

ABSTRACT

This paper considers scattering screens that have arbitrary spatial variations of scattering strength transverse to the line of sight, including screens that are spatially well confined, such as disks and filaments. We calculate the scattered image of a point source and the observed pulse shape of a scattered impulse. The consequences of screen confinement include: (1) Source image shapes that are determined by the physical extent of the screen rather than by the shapes of much-smaller diffracting microirregularities. These include image elongations and orientations that are frequency dependent. (2) variation with frequency of angular broadening that is much weaker than the trademark ν^{-2} scaling law (for a cold, unmagnetized plasma), including frequency-independent cases; and (3) similar departure of the pulse broadening time from the usually expected ν^{-4} scaling law. We briefly discuss applications that include scattering of pulses from the Crab pulsar by filaments in the Crab Nebula; image asymmetries from Galactic scattering of the sources Cyg X-3, Sgr A*, and NGC 6334B; and scattering of background active galactic nuclei by intervening galaxies. We also address the consequences for inferences about the shape of the wavenumber spectrum of electron density irregularities, which depend on scaling laws for the image size and the pulse broadening. Future low-frequency (< 100 MHz) array observations will also be strongly affected by the Galactic structure of scattering material. Our formalism is derived in the context of radio scattering by plasma density fluctuations. It is also applicable to optical, UV and X-ray scattering by grains in the interstellar medium.

Subject headings: ISM: structure — pulsars: general — scattering

1. Introduction

Images of scattered radio sources and distorted pulses from pulsars provide some of the most-used observables for probing microstructure in the electron density of interstellar gas. Over the last decade, interstellar scattering measurements have revealed asymmetries in the scattered images of radio sources. These are most often interpreted in terms of underlying anisotropy of

the very small irregularities that diffract the radiation. That anisotropy, in turn, most likely reflects the orientation of magnetic fields in the H II gas that contains the microstructure. Angular broadening of compact sources and pulse distortions due to multi-path propagation are used to probe the amplitude of scattering and also, through the frequency scaling, to constrain the shape of the wavenumber spectrum for the microstructure. Inversion of scattering observables into information about the microstructure almost invariably relies on the assumption that the scattering strength is uniform in directions transverse to the line of sight.

We reconsider the assumptions used to analyze angular and temporal broadening, in particular the assumption of uniformity of the scattering medium transverse to the line of sight. One reason is that the interstellar medium (ISM) shows structures on a wide variety of scales and so it is reasonable to expect manifestations of nonuniformities, at least in some directions. Secondly, the physics that underlies asymmetric images is quite different if the asymmetry occurs on scales much larger than diffractive scales, as they would if the asymmetry is caused by the large-scale distribution of diffracting irregularities. Thirdly, observations of the Crab pulsar show anomalous scalings of pulse broadening with frequency. These are interpreted by some as indicating that scattering occurs within the pulsar magnetosphere rather than in a cold plasma (J. Eilek 1997, private communication; Hankins & Moffett 1998; Lyutikov & Parikh 2000). As we show, anomalous scalings occur quite naturally from cold plasma extrinsic to the pulsar if the scattering region is bounded in the transverse direction. Additionally, future observations at low radio frequencies of a variety of sources – including high redshift sources – are expected to reveal further anomalous scattering that most likely will be the result of confined scattering structures. Finally, the scaling with frequency of angular and pulse broadening is often used to constrain the shape of the wavenumber spectrum of scattering irregularities (e.g., Cordes, Weisberg, & Boriakoff 1985; Fey et al. 1991). Weakening of the frequency dependence by confined plasma structures would be interpreted as a steeper wavenumber spectrum. Thus it is important to assess the role of confined structures in the observations of scattered radio sources.

In §2 we discuss previous treatments of angular and pulse broadening. In §3 we derive a general formalism for scattering that takes into account arbitrary variations of scattering strength transverse to the line of sight. Examples are given in §4. Applications to the Crab pulsar and other Galactic sources are given in §5. Future observations of extragalactic sources and at low frequencies are considered in §6. In §7 we discuss possible implications for the interstellar medium. Finally, in §8, we summarize our results.

2. Past Treatments of Angular and Pulse Broadening

It is well known that the shape of a scattered impulse, viewed through a thin (along the line of sight), infinitely-extended (transverse to the line of sight) screen with a circularly symmetric, Gaussian angle distribution, is a one-sided exponential function (e.g., Rickett 1990 and references therein). Thick scattering screens produce slower rise times, while screens containing Kolmogorov

irregularities (e.g., Rickett 1990; Lambert & Rickett 1999) produce decays that are slower than exponential. Results along these lines have been presented by Scheuer (1968), Williamson (1972, 1973, 1975), Lee & Jokipii (1975), and Isaacman & Rankin (1977). Williamson (1975) has shown that the pulse broadening function from multiple, discrete screens or from a continuous medium consists of an n -fold convolution of (one-sided) exponential functions. Williamson’s result applies to the case where the phase structure function is square-law in form. Media with Kolmogorov wavenumber spectra produce different shapes, though the differences are small compared to effects we consider in this paper. The key, implicit assumption in Williamson’s analysis (and essentially all other published results on interstellar pulse broadening; however, see Lyne & Thorne 1975) is that the transverse extent of the scattering screen is arbitrarily large and that the strength of scattering is uniform across the screen. If these assumptions are relaxed, quite different results emerge.

We show that several “anomalous” phenomena occur when scattering structures have finite transverse extents, including:

1. Angular broadening from scattering or refraction that scales anomalously with ν . In the case of radio scattering in cold plasmas, anomalous scaling is defined as a significant departure from a ν^{-2} scaling, which is determined by the microphysics of the plasma.¹ Departures will always consist of a *weaker* dependence on frequency.
2. Elongated (or otherwise distorted) images of point sources that are due to scattering but do not scale as ν^{-2} .
3. Multiple imaging by multiple, discrete screens with image intensities influenced by dilution from scattering.
4. Temporal broadening of pulsar pulses which shows a *weaker* dependence on frequency than ν^{-4} , in accord with the scaling of angular broadening.²
5. Replication of pulses by multiple imaging from an ensemble of screens.

The goal of this paper is to discuss the impact of confined or heavily modulated scattering screens on some of the basic observables, primarily pulse broadening and angular broadening. Therefore we do not explicitly consider refraction from large scale features in the ISM. We do so for two reasons. First, purely diffractive effects are rich enough in variety that we need to isolate the

¹ Scattering from irregularities with a Kolmogorov wavenumber spectrum shows $\nu^{-11/5}$ scaling under the circumstance of moderate scattering (cf. Cordes & Lazio 1991). We do not consider this scaling anomalous. When a confined structure contains Kolmogorov fluctuations, the scaling of angular size may be considerably shallower than $\nu^{-11/5}$.

² A Kolmogorov spectrum can show a $\nu^{-22/5}$ scaling for pulse broadening. As with angular broadening, we do not consider this anomalous.

discussion to those effects. Secondly, our results can also be applied to some cases where refraction is important by considering a “renormalized” version of the Kirchoff diffraction integral (e.g., Cordes, Pidwerbetsky & Lovelace 1986). Renormalization of the large scale gradient and phase curvature caused by refraction at a given screen location can be cast as an increased or decreased image intensity and also as a change in the ellipticity of the angular distribution of scattered radiation. In the following we use a probability density, $f\mathbf{a}$, to describe the scattering angles \mathbf{a} from a screen. The renormalization approach allows some of the effects of refraction — image shifts and shapes and intensity changes — to be absorbed into $f\mathbf{a}$. Our approach considers only geometrical path length contributions to arrival times and excludes dispersive delays, which are associated with the screen itself. For some situations, dispersive delays can be important. In this paper, the points that we wish to make concern the geometrical phase and a complete discussion that includes dispersive delays would distract our discussion of these points. Consequently, we defer to another paper a complete treatment that includes all contributions to arrival times.

3. Probability Densities for Angle of Arrival and Time of Arrival

We derive the image of a scattered point source and the scattered pulse shape of an impulse by calculating, respectively, the probability density functions (PDFs) for the angle of arrival (AOA) and the time of arrival (TOA). In the following, we calculate the effects of scattering while using some of the language and mathematics of ray theory. Williamson (1975) has shown the equivalence of wave and ray optics for some contexts, as have Cordes & Rickett (1998). In this paper, we make the simplifying assumption that the TOA is related geometrically to the AOA. This relationship applies when only the geometrical path length of a given ray path contributes significantly to the TOA. In general, the TOA includes another term related to the integrated refractive index (the integrated electron density in the case of a cold plasma). We ignore the non-geometrical term because there are astrophysical contexts where its contribution is negligible.

Consider a series of diffracting screens at distances D_{s_j} from a source that is at distance D from the observer. Letting \mathbf{a}_j be the (two-dimensional) scattering angle from the j th screen, the angular deviation $\boldsymbol{\theta}(s)$ of a ray path and its transverse offset $\mathbf{x}(s)$ from the direct ray path at distance s from the source are

$$\boldsymbol{\theta}(s) = \boldsymbol{\theta}_i + \sum_j \mathbf{a}_j U(s - D_{s_j}) \quad (1)$$

$$\mathbf{x}(s) = s\boldsymbol{\theta}_i + \sum_j (s - D_{s_j})\mathbf{a}_j U(s - D_{s_j}), \quad (2)$$

where $U(x)$ is the unit step function. The first equation relates the observed ray angle ($\boldsymbol{\theta}$) to the initial ray angle ($\boldsymbol{\theta}_i$) and the scattering angles (\mathbf{a}_j). The relation $\mathbf{x}(D) = 0$ stipulates that rays must reach the observer. We assume all angles are small ($|\boldsymbol{\theta}_i|, |\mathbf{a}_j|, |\boldsymbol{\theta}| \ll 1$), though it is not difficult to extend our results to large angles. Note that \mathbf{a}_j is a random variable described by a

distribution of angles that is determined by diffraction (and, as mentioned above, can also include refraction).

Including only the geometric path-length difference, the corresponding time delay relative to the direct ray path is

$$t = \frac{1}{2c} \int_0^D ds |\boldsymbol{\theta}(s)|^2. \quad (3)$$

The overall time delay also includes dispersive components which, as stated above, we choose to ignore because our main points concern the effects of truncated screens on the arrival times.

To calculate the probability density function (PDF) of the observed angle of arrival, $\boldsymbol{\theta}$, and the time of arrival, t , we use Dirac delta functions to enforce Eq. 1 and $\mathbf{x}(D) = 0$ for those rays that reach the observer. We use conditional probabilities to include these relations and to integrate over the PDFs for the scattering angles in each screen and over the PDF of $\boldsymbol{\theta}_i$. The result is simple for an isotropic source or, less restrictively, where the PDF of $\boldsymbol{\theta}_i$ is constant over the relevant range of initial ray angles, $\boldsymbol{\theta}_i$, as we assume. Note that the equation $\mathbf{x}(D) = 0$ allows us to eliminate $\boldsymbol{\theta}_i$ as an independent variable.

It is standard to assume the scattering strength is invariant across a scattering screen. Here we specify a more general description. Consider each screen to scatter or refract rays according to a PDF $f_{\mathbf{a}_j}$ whose width varies arbitrarily across the screen. Accordingly we write each screen's PDF as $f_{\mathbf{a}_j}(\mathbf{a}_j; \mathbf{x}(D_{s_j}))$, where $\mathbf{x}(D_{s_j})$ is Eq. 2 evaluated at the location of each screen, $s = D_{s_j}$.

Let Q be an observed quantity such as the AOA or TOA and let $Q'(\boldsymbol{\theta}_i, \mathbf{a}_j, D_{s_j}, D)$ be its value given $\boldsymbol{\theta}_i$, \mathbf{a}_j and D_{s_j} (and it is implicit that we consider all j when there are multiple screens). The PDF of Q is

$$f_Q(Q) = \frac{\prod_j \int d\mathbf{a}_j f_{\mathbf{a}_j}(\mathbf{a}_j; \mathbf{x}(D_{s_j})) \int d\boldsymbol{\theta}_i f_{\boldsymbol{\theta}_i}(\boldsymbol{\theta}_i) \delta(\mathbf{x}(D)) \delta(Q - Q'(\boldsymbol{\theta}_i, \mathbf{a}_j, D_{s_j}, D))}{\prod_j \int d\mathbf{a}_j f_{\mathbf{a}_j}(\mathbf{a}_j; \mathbf{x}(D_{s_j})) \int d\boldsymbol{\theta}_i f_{\boldsymbol{\theta}_i}(\boldsymbol{\theta}_i) \delta(\mathbf{x}(D))}, \quad (4)$$

where the numerator is the joint PDF of Q and $\mathbf{x}(D) = 0$ (that rays reach the observer), while the denominator is the PDF that rays reach the observer. Using Eq. 2, we transform $\delta(\mathbf{x}(D))$ to a delta function involving $\boldsymbol{\theta}_i$, perform the integral over $\boldsymbol{\theta}_i$, and assume that the PDF for $\boldsymbol{\theta}_i$, $f_{\boldsymbol{\theta}_i}$, is constant for angles of interest. Then Q' becomes independent of $\boldsymbol{\theta}_i$ and the PDF of Q becomes

$$f_Q(Q) = \frac{\prod_j \int d\mathbf{a}_j f_{\mathbf{a}_j}(\mathbf{a}_j; \mathbf{x}(D_{s_j})) \delta(Q - Q'(\mathbf{a}_j, D_{s_j}, D))}{\prod_j \int d\mathbf{a}_j f_{\mathbf{a}_j}(\mathbf{a}_j; \mathbf{x}(D_{s_j}))}. \quad (5)$$

3.1. The General Single Screen (N=1)

For the simple case of a single scattering screen, Eq. 5 becomes

$$f_Q(Q) = \frac{\int d\mathbf{a} f_{\mathbf{a}}(\mathbf{a}; -\mathbf{a}D'_s) \delta(Q - Q'(\mathbf{a}, D_s, D))}{\int d\mathbf{a} f_{\mathbf{a}}(\mathbf{a}; -\mathbf{a}D'_s)}, \quad (6)$$

where

$$D'_s = D_s(1 - D_s/D). \quad (7)$$

For the angle of arrival, $Q = \theta$, $Q' = \mathbf{a}(D_s/D)$ and

$$f_{\theta}(\theta) = \left(\frac{D}{D_s}\right)^2 \frac{f_{\mathbf{a}}\left(\frac{D}{D_s}\theta; -\theta(D - D_s)\right)}{\int d\mathbf{a} f_{\mathbf{a}}(\mathbf{a}; -\mathbf{a}D'_s)}. \quad (8)$$

For the TOA, $Q = t$ and $Q' = D_s(1 - D_s/D)|\mathbf{a}|^2/2c$ so only the magnitude, $|\mathbf{a}|$, is constrained. Transformation of $\delta(Q - Q')$ to $\delta(|\mathbf{a}| - a_t)$ yields

$$f_t(t) = \left(\frac{c}{D'_s}\right) \frac{\int_0^{2\pi} d\phi f_{\mathbf{a}}(a_t \hat{\mathbf{a}}_{\phi}; -a_t \hat{\mathbf{a}}_{\phi} D'_s)}{\int d\mathbf{a} f_{\mathbf{a}}(\mathbf{a}; -\mathbf{a}D'_s)}, \quad (9)$$

where $\hat{\mathbf{a}}_{\phi}$ is a unit vector,

$$\hat{\mathbf{a}}_{\phi} = \cos \phi \hat{\mathbf{x}} + \sin \phi \hat{\mathbf{y}}, \quad (10)$$

and

$$a_t = \left(\frac{2ct}{D'_s}\right)^{1/2}. \quad (11)$$

The flux density of a source is conserved only for an infinite screen with homogeneous statistics because only in that case is as much flux scattered toward the observer as is scattered away. We define the flux dilution factor as the ratio of the probability that rays reach the observer to the probability for a uniform, infinite screen:

$$\eta_F = \int d\mathbf{a} f_{\mathbf{a}}(\mathbf{a}; -\mathbf{a}D'_s), \quad (12)$$

equal to the denominator of Eq. 6. For a uniform, infinite screen, $\eta_F = 1$. In general, $\eta_F \leq 1$.

We illustrate these expressions by considering specific cases.

3.1.1. Infinitely Wide Screen with Homogeneous Statistics

For an infinite screen with homogeneous statistics, the denominator of Eq. 6 is unity. Specializing to circularly symmetric $f_{\mathbf{a}}$, we find the normalized 1D PDF for the magnitude $\theta \equiv |\boldsymbol{\theta}|$:

$$f_{\theta}(\theta) = 2\pi\theta \left(\frac{D}{D_s}\right)^2 f_{\mathbf{a}}(D\boldsymbol{\theta}/D_s). \quad (13)$$

If $f_{\mathbf{a}}$ is a Gaussian function with rms angle σ_a in each coordinate direction, then

$$f_{\theta}(\theta) \approx \sigma_{\theta}^{-2} \theta e^{-\theta^2/2\sigma_{\theta}^2} \quad (14)$$

$$\sigma_{\theta} \equiv (D_s/D)\sigma_a \quad (15)$$

$$f_t(t) = \tau_0^{-1} e^{-t/\tau_0} U(t) \quad (16)$$

$$\tau_0 = D'_s \sigma_a^2 / c. \quad (17)$$

The 1D rms angle

$$\theta_{\text{rms}} \equiv \frac{1}{\sqrt{2}} \langle |\boldsymbol{\theta}|^2 \rangle^{1/2} \quad (18)$$

characterizes the *observed* range of angles and in this case is identical to σ_{θ} , which is the scaled range of *scattering* angles. In general, $\theta_{\text{rms}} \neq \sigma_{\theta}$.

If $\sigma_a \propto \nu^{-2}$ as for a plasma, then the AOA PDF has a scale $\sigma_{\theta} \propto \nu^{-2}$ and the TOA PDF has scale $\tau_0 \propto \nu^{-4}$. These scaling laws for observable quantities rely on the assumption that the screen is infinitely wide.

3.1.2. Circular Screen with Finite Radius

Consider a circular screen with radius X_{max} centered on the line of sight. Now the PDF for θ is truncated for $\theta > \theta_{\text{max}} \equiv X_{\text{max}}/(D - D_s)$. Again adopting circularly symmetric, Gaussian statistics for \mathbf{a} , we find

$$f_{\theta}(\theta) = [\sigma_{\theta}^2(1 - e^{-\zeta})]^{-1} \theta e^{-\theta^2/2\sigma_{\theta}^2} U(\theta_{\text{max}} - \theta), \quad (19)$$

$$\zeta \equiv \frac{1}{2} \left(\frac{\theta_{\text{max}}}{\sigma_{\theta}}\right)^2, \quad (20)$$

where the unit step function enforces truncation of the PDF for $\theta > \theta_{\text{max}}$. If the rms scattering angle is small, $\sigma_a \ll X_{\text{max}}D/D_s(D - D_s)$, the scaling of the observed size with frequency is according to that of σ_a . For larger scattering angles, the physical size of the screen becomes important. To see this, we calculate the rms angular size, which is, for the circularly symmetric Gaussian and a frequency scaling $\sigma_a = \sigma_{a0}(\nu/\nu_0)^{-2}$,

$$\theta_{\text{rms}} = \sigma_{a0} \left(\frac{D_s}{D}\right) \left(\frac{\nu}{\nu_0}\right)^{-2} \left[\frac{1 - (1 + \zeta)e^{-\zeta}}{1 - e^{-\zeta}} \right]^{1/2}. \quad (21)$$

The frequency scaling is $\zeta \propto \nu^4$. At large ν , $\zeta \gg 1$ and $\theta_{\text{rms}} \propto \nu^{-2}$. At small ν , $\zeta \rightarrow 0$ and θ_{rms} becomes frequency independent.

The TOA has a PDF and mean value

$$f_t(t) = \frac{e^{-t/\tau_0}}{\tau_0(1 - e^{-\zeta})} U(t_{\text{max}} - t) \quad (22)$$

$$\langle t \rangle = \tau_0 \left[1 - \zeta \left(\frac{e^{-\zeta}}{1 - e^{-\zeta}} \right) \right] \quad (23)$$

$$t_{\text{max}} = \zeta \tau_0. \quad (24)$$

For a wide screen, $\zeta \rightarrow \infty$, $t_{\text{max}} \rightarrow \infty$ and $\langle t \rangle = \tau_0$, as before. However, a narrow screen with $\zeta \ll 1$ gives $\langle t \rangle \sim \zeta \tau_0$. The TOA scaling is $\langle t \rangle \propto \nu^{-4}$ for wide screens but becomes frequency independent for very narrow screens.

The observed flux of a source viewed through the truncated screen is attenuated by the scattering. The flux dilution factor is

$$\eta_F = 1 - e^{-\zeta}. \quad (25)$$

For $\zeta \ll 1$, $\eta_F \sim \zeta$ while $\zeta \gg 1$ yields $\eta_F = 1$. When the angular diameter and pulse broadening of a source are observed to have anomalous frequency dependence, i.e., when scattering is dominated by a truncated screen, the flux is diminished. Inspection of Eq. 21 and Eq. 25 indicates that there can be a correlation of rms angular size and flux density.

3.2. A Screen with Arbitrary Variations of Scattering Strength

Above, we considered screens with extreme variations of scattering strength: discontinuous or truncated to zero. Here we consider other cases that may have relevance to sources that are viewed through scattering regions with structure on scales $\sim (D - D_s)\theta$. As in Eq. 5, we specify the scattering angle \mathbf{a}_j from the j th screen by a PDF that depends on location along the screen, $\mathbf{x}(D_{s_j})$: $f_{\mathbf{a}_j}(\mathbf{a}_j; \mathbf{x}(D_{s_j}))$. For simplicity, we drop the j subscripts and discuss scattering from a single screen. Also, for ease of discussion, we consider $f_{\mathbf{a}}$ to be a 2D Gaussian with angular variance $\sigma_{\mathbf{a}}(\mathbf{x})$ that varies across the screen.

In some circumstances, the angle-of-arrival distribution f_{θ} is determined purely by the shape and width of $f_{\mathbf{a}}$, while in others it is determined by the variations in $\sigma_{\mathbf{a}}$ across the screen. If $\sigma_{\mathbf{a}}$ is constant across the screen, f_{θ} is a scaled version of $f_{\mathbf{a}}$ and the frequency scaling of the observed angular size is identical to that of the scattering angles.

However, if $\sigma_{\mathbf{a}}$ varies across the screen, the observed angular size may reflect variations of $\sigma_{\mathbf{a}}$ in addition to or rather than the width of $f_{\mathbf{a}}$ itself. Let $\ell_{\mathbf{a}}$ be the characteristic length scale on which $\sigma_{\mathbf{a}}$ varies across the screen. We compare this with the observed angular diameter projected back to the screen, yielding a length scale $\ell_{\perp} \sim (D - D_s)\theta_{\text{rms}}$. We consider three cases:

1. If $\ell_{\mathbf{a}} \ll \ell_{\perp}$ and variations in $\sigma_{\mathbf{a}}$ are statistically homogeneous, the variations average out. The scaling with frequency of the observed AOA width is identical to that of \mathbf{a} , which is due to the microphysics. Note that our examples of truncated screens in previous sections satisfy the inequality but are not statistically homogeneous.
2. If $\ell_{\mathbf{a}} \gg \ell_{\perp}$, then $\sigma_{\mathbf{a}} \approx \text{constant}$ over the part of the screen sampled and the angle-of-arrival PDF is determined by $f_{\mathbf{a}}$. The frequency scaling is again determined by the microphysics. Depending on how large $\ell_{\mathbf{a}}$ is, eventually time variations in the image are expected on a time scale $t_a \sim \ell_{\mathbf{a}}/V_{\text{eff}}$, where V_{eff} is an effective velocity determined by the velocities of the source, medium and observer (e.g., Cordes & Rickett 1998).
3. If $\ell_{\mathbf{a}} \sim \ell_{\perp}$, the AOA PDF is determined by a combination of $f_{\mathbf{a}}$ and the spatial variation of $\sigma_{\mathbf{a}}$. The truncated screen of §3.1.2 is an extreme example of this case. The frequency scaling is likely to depart significantly from that of the microphysics.

4. Examples

4.1. Illustration of Anomalous Frequency Scaling

Figure 1 shows the “image” f_{θ} , the pulse broadening function f_t , and the scaling with frequency of the pulse broadening time for two cases: (a) an infinite screen (bold solid lines) and (b) a truncated circular screen centered on the direct line of sight (light and dashed lines). The underlying scattering function ($f_{\mathbf{a}}$) is a circular Gaussian PDF and the rms scattering angle scales as ν^{-2} . For the infinite screen, the pulse broadening scales as ν^{-4} , as expected. However, the truncated screen yields truncated images and truncated pulse broadening functions if the rms scattering angle is large enough that rays from the screen’s edges reach the observer. Thus, truncation occurs at low frequencies and not at high frequencies. For the example given, the break frequency ~ 0.5 GHz. Actual break frequencies will depend on particular sizes and scattering strengths of screens.

As a second illustration of anomalous frequency scaling, we calculate the pulse broadening for a pulse scattered by a two component screen. The first, circular component with radius X_1 is centered on the line of sight and scatters radiation much more strongly than the remainder of the screen, which is of infinite extent. The distributions of AOA and TOA follow from the master equations, Eq. 8,9. The rms angular size, the mean TOA, and related quantities are:

$$\theta_{\text{rms}} = \sqrt{2} \sigma_{\text{d1}} \left(\frac{D_s}{D} \right) \left[\frac{1 + (\tau_2/\tau_1)(1 + \zeta_2)e^{-\zeta_2} - (1 + \zeta_1)e^{-\zeta_1}}{1 + e^{-\zeta_2} - e^{-\zeta_1}} \right]^{1/2} \quad (26)$$

$$\langle t \rangle = \tau_1 \left[\frac{1 + (\zeta_1 + \tau_2/\tau_1)e^{-\zeta_2} - (1 + \zeta_1)e^{-\zeta_1}}{1 + e^{-\zeta_2} - e^{-\zeta_1}} \right] \quad (27)$$

$$\tau_{1,2} = c^{-1} D'_s \sigma_{\text{d1,2}}^2 \quad (28)$$

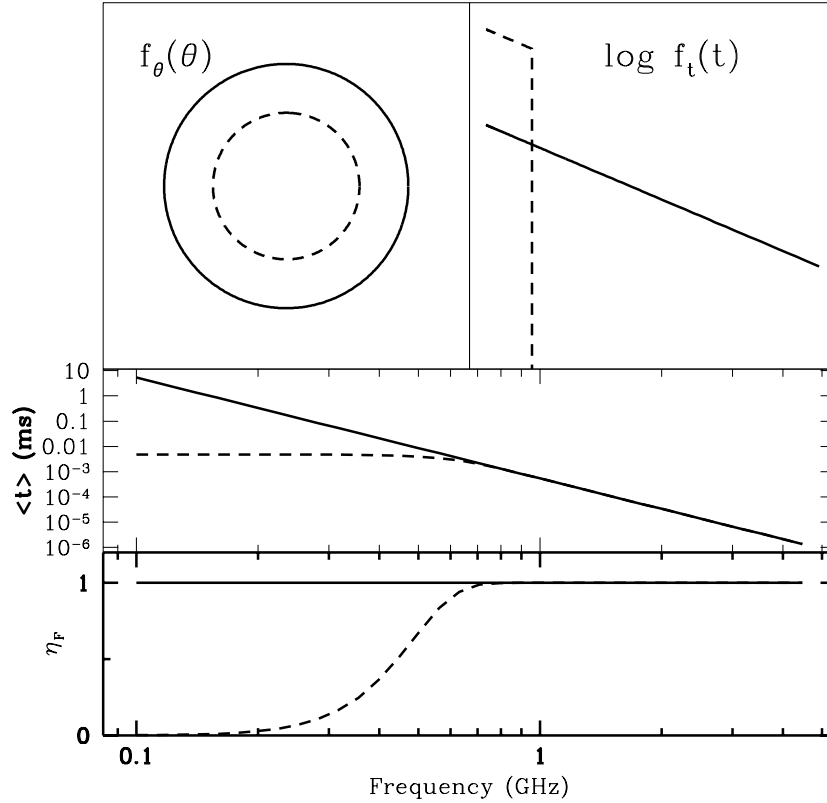


Fig. 1.— Scattering from an infinite screen (solid lines) and a truncated circular screen of radius 6 mas (dashed lines). Top left: image contours for an rms angle $\sigma_\theta = 10$ mas. For the infinite screen, the contour is at 1σ of the Gaussian profile; for the truncated screen, the contour represents the sharp edge of the screen. Top right panel: pulse broadening functions on a log-linear scale. Middle panel: mean pulse broadening times plotted against frequency for $\sigma_\theta = 1$ mas at 1 GHz, $D_s = 0.33$ kpc, and $D = 1$ kpc. Bottom panel: flux dilution factors, η_F .

$$\zeta_1 = \frac{1}{2} \left[\frac{X_1}{D'_s \sigma_{d1}} \right]^2 \tag{29}$$

$$\zeta_2 = \frac{\tau_1}{\tau_2} \zeta_1, \tag{30}$$

where $\sigma_{d1,2}$ is the rms scattering angle produced by each screen.

Figure 2 shows θ_{rms} plotted against frequency for different ratios, σ_{d1}/σ_{d2} and assuming that $\sigma_{d1,2} \propto \nu^{-2}$. Note that we vary σ_{d1}/σ_{d2} while keeping σ_{d1} constant. The figure demonstrates how the stronger central component dominates the apparent source size at high frequencies and the weaker, distributed component dominates at low frequencies. At intermediate frequencies, there is a plateau where the angular size is nearly independent of frequency.

Figure 3 shows a similar plot, now for the mean pulse broadening time, $\langle t \rangle$, plotted against frequency for different ratios, τ_1/τ_2 and assuming that $\sigma_{d1,2} \propto \nu^{-2}$. The roles of the central and distributed components are the same as for the angular scattering shown in Figure 2.

4.2. Scattering from Filaments

Figure 4 shows scattering from a filament located along the direct ray path for three values of rms scattering angle in the filament. Small rms scattering yields a circular image and an exponential pulse broadening function. For sufficiently large scattering angles, the image becomes elongated and tends toward a $t^{-1/2}e^{-t}$ pulse broadening function

Figure 5 shows scattering from a filament at different locations relative to the direct ray path but for identical rms scattering angles in the filament. When the filament is near enough to the image center, the pulse broadening function is bimodal. When the filament is far, the pulse broadening function is dominated by the much weaker scattering from outside the filament. Clearly, a superposition of filaments near the direct ray would produce a multiplicity of pulses.

Figure 6 shows scattering from an ensemble of filaments at different frequencies. As can be seen, the pulse broadening function shows multiple peaks that align at different frequencies. The number of filaments that are ‘lit up’ by the scattering decreases in going to higher frequency. The scattering screen consists of a very strong, extended component which has embedded “gaps” where the scattering is weaker but still strong enough to scatter radiation toward the observer. The extended component scatters radiation to such wide angles that it produces negligible contributions to the pulse broadening function and to the image. Thus the strongest contributions to measured quantities come from the filamentary gaps. We will explore this result further in a separate paper to discuss giant pulses from the Crab pulsar.

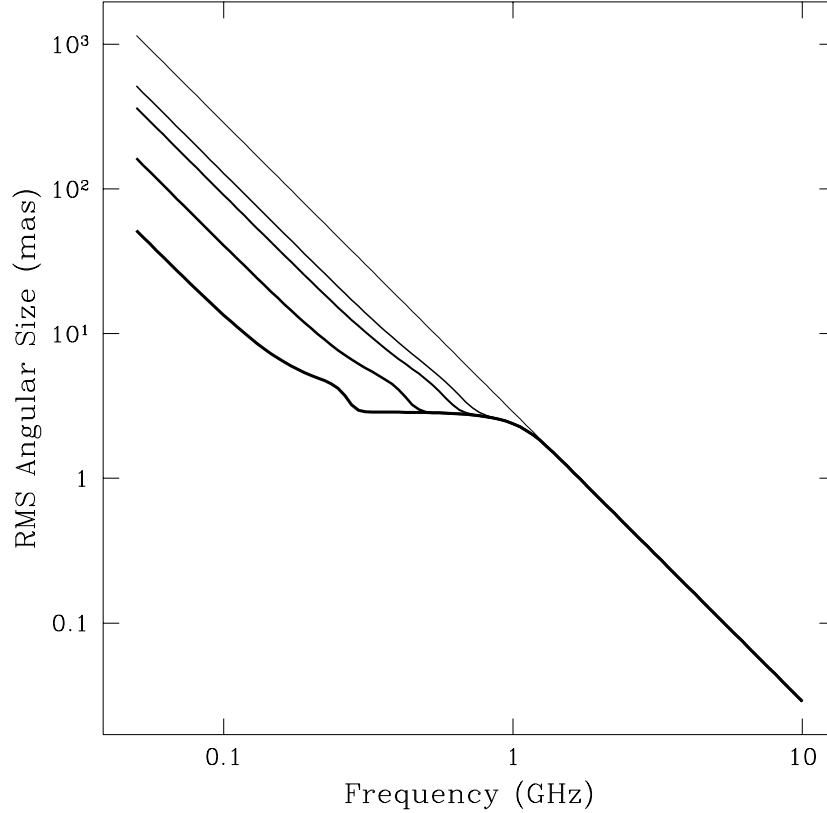


Fig. 2.— RMS angular size plotted against frequency for a two component scattering screen, with a strongly scattering central part and a more weakly scattering extended part. The curves are evaluations of Eq. 26 and correspond to different ratios, $\sigma_{d1}/\sigma_{d2} = 500, 50, 10, 5, 1$ in order of thickest to thinnest lines, where σ_{d1} is the rms scattering angle from the central part and σ_{d2} is the value for the extended part. In producing this figure, we have varied σ_{d1}/σ_{d2} while keeping σ_{d1} constant. The wavy features in some of the curves are real and reflect the different frequency dependences of terms that are subtracted in the expression for rms angular size.

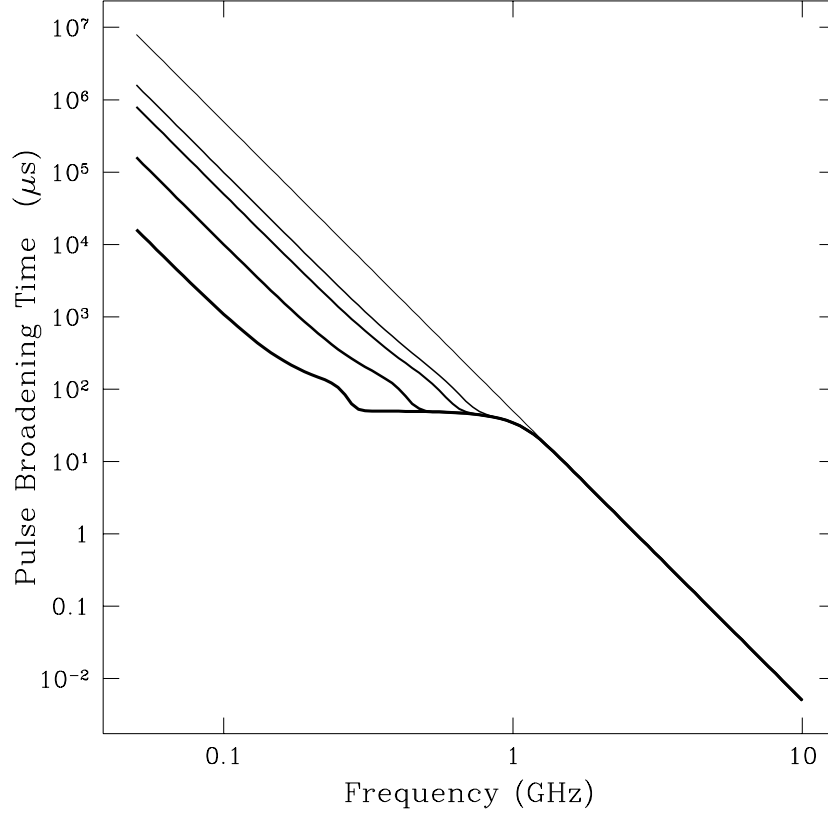


Fig. 3.— Pulse broadening time plotted against frequency for a two component scattering screen, with a strongly scattering central part and a more weakly scattering extended part. The curves are evaluations of Eq. 27 and correspond to different ratios, $\tau_1/\tau_2 = 500, 50, 10, 5, 1$ in order of thickest to thinnest lines, where τ_1 is the pulse broadening time of the central part (if it were infinite in extent) and τ_2 is the value for the extended part.

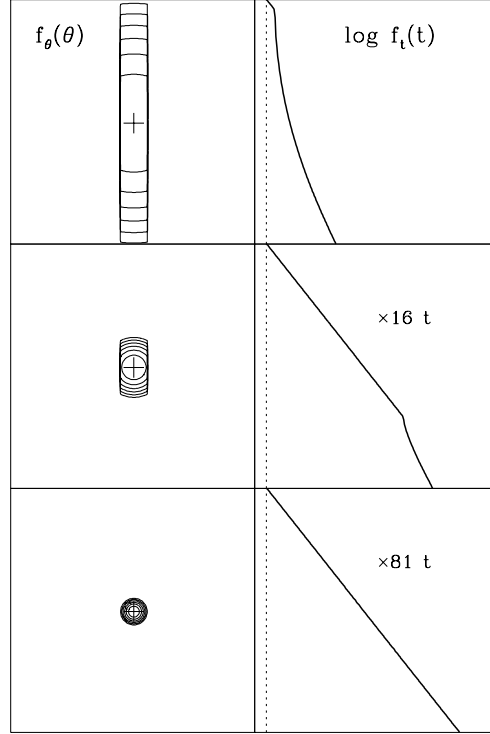


Fig. 4.— Images and pulse broadening functions for a vertical filament centered on the direct line of sight but with different rms scattering angles. The filament has a width of 0.28 mas, a length of 300 mas and truncates sharply. Equations 8,9 were evaluated to obtain the plots. Left panels: Images shown on a frame of size 2.5×2.5 mas. The ‘+’ symbol designates the direct line of sight to the source. The rms scattering angle is constant in the filament and is $1 \text{ mas } \nu^{-2} = 1, 0.25,$ and 0.11 mas for $\nu = 1, 2,$ and 3 GHz in going from the top to the bottom frame. The contour levels extend from the maximum down to 10^{-3} of the maximum in uniformly spaced intervals of one half decade. Right panels: The pulse broadening function is shown on a log-linear scale with 1 decade on the vertical axis. The horizontal axis extends to $1.5 \mu\text{s}$ in the top frame and to factors of 16 and 81 times smaller in the middle and lowest panels to compensate for the ν^{-4} dependence of the pulse broadening time (if there were a continuous screen). The vertical dashed line indicates zero delay. Top: Large rms scattering angle so that the image shape is dominated by the edges of the filament. The pulse broadening function is nearly of the form $t^{-1/2}e^{-t}$. Middle: Smaller rms scattering angle so that the image is less elongated. The pulse broadening function is exponential at small delays but shows a break point because there is an absence of large delays due to the truncation of the filament. Bottom: Rms scattering angle small enough so that the edges of the filament are not seen. The pulse broadening function is exponential in form, e^{-t} .

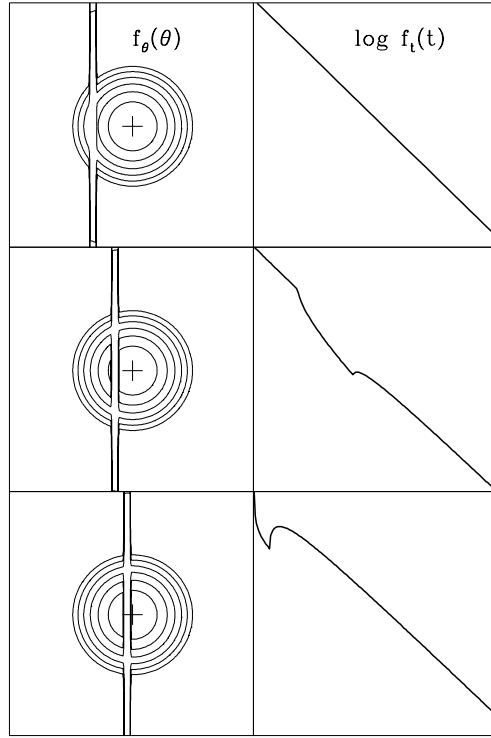


Fig. 5.— Images and pulse broadening functions for a filament at different locations from the direct line of sight, evaluated using Eq. 8-9. The filament is 0.075 mas wide and 300 mas long and the rms scattering angles are 4 and 0.5 mas inside and outside the filament, respectively. Left panels: Images of size 2.5×2.5 mas shown with contours spaced at half-decade intervals down to 10^{-3} from the peak. The ‘+’ symbol designates the direct line of sight to the source. Right panels: pulse broadening functions shown on log-linear scales; the vertical axis covers one decade and the horizontal axis covers $0.3 \mu\text{s}$. (Top) The image is a circular Gaussian combined with a subimage from the filament. The filamentary subimage is weaker in amplitude because flux is diluted by the heavier scattering from the filament. The pulse broadening function is nearly exponential in form, $\propto e^{-t}$. (Middle) The filament is close enough so that its subimage now contributes significantly to the pulse broadening function, which is distorted by the depletion of flux at some delays by the scattering from the filament. (Bottom) The circular and filamentary subimages are sufficiently merged so that the pulse broadening function is bimodal: a narrow component from the portion of the filament nearest the direct line of sight and a second peak associated with the nonfilamentary scattering. Relative to the peak, the pulse broadening function is now slightly broader than in the top and middle cases.

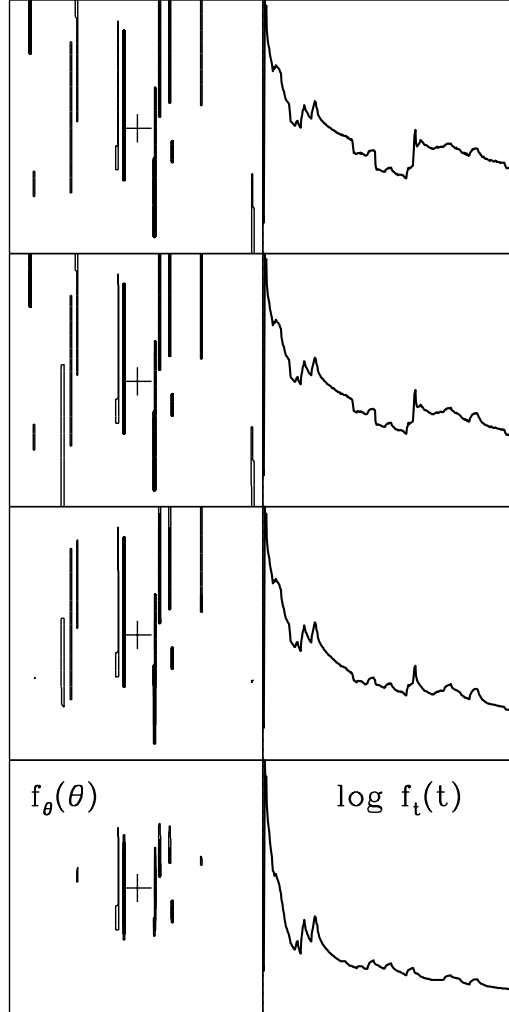


Fig. 6.— Images and pulse broadening functions for an ensemble of filaments superposed with a much stronger scattering screen. The filaments therefore represent ‘gaps’ where the scattering is weaker than in the screen, but still strong enough to scatter radiation back to the observer. Physical filament widths and lengths are 0.03 mas and 1.5 mas, respectively, though their apparent lengths are smaller because the flux scattered to the observer depends on distance from the direct ray path. At 1 GHz, the screen has an rms scattering angle of 2 mas while the filaments have scattering angles assigned randomly and uniformly between 0.1 and 2 mas. Scattering angles scale as ν^{-2} . From top to bottom, $\nu = 0.1, 0.2, 0.3$ and 0.5 GHz. Left panels: images are shown in 2.5×2.5 mas frames with contours spaced at half-decade intervals over 1 decade from the image peaks. Contributions from the strong screen are too small to be reflected in the contours. Right panels: pulse broadening functions shown on a log linear scale with one decade on the vertical axis. The horizontal axis covers $6.7 \mu\text{s}$. The observed shapes are dominated by the filamentary gaps.

5. Application to Galactic Scattering

Galactic sources show a wide range of scattering levels, indicative of the concentration of intense scattering into a Population I type Galactic distribution (Cordes, Weisberg, & Boriakoff 1985 ; Taylor & Cordes 1993). Here we discuss particular objects whose scattering may be interpreted in the context of this paper’s formalism. Our discussion is brief. We defer to separate articles any detailed treatment on particular sources.

5.1. The Crab Pulsar

The Crab pulsar shows enhanced pulse broadening from nebular material that has been recognized since shortly after the pulsar’s discovery in 1968 (e.g., Vandenburg 1976 and references therein). The nebular contribution is highly episodic, with dramatic increases of the pulse broadening time by a factor of 100 (Lyne & Thorne 1975; Isaacman & Rankin 1977). Recently, multiple images have been inferred from the presence of echoes of the pulse shape (Graham Smith & Lyne 2000; Backer 2000; Backer, Wong, & Valanju 2000).

Giant pulses from the Crab pulsar show additional evidence for nebular contributions to the scattering that are probably from discrete filaments. At relatively high frequencies (1.4 to 5 GHz), giant pulses show multiple pulse components that tend to have exponential scattering tails with time constants that often differ, even within the same spin period of the pulsar (Hankins & Moffett 1998; Sallmen et al. 1999; Hankins 2000). Also, the widths of the pulse components appear to scale less strongly with frequency than ν^{-4} . These characteristics suggest consistency with the overall picture developed in this paper. A detailed analysis of the Crab pulsar’s pulses is deferred to another paper.

5.2. NGC 6334B

The largest angular broadening measured is for the extragalactic source NGC 6334B viewed through the H II complex NGC 6334 (Trotter, Moran, & Rodríguez 1998 and references therein), $\theta_d \approx 3''$ at 1.4 GHz. The image’s position angle rotates in going from low to high frequency, and the image axial ratio may increase from 1.2 at 1.4 and 5 GHz to 1.5 at 15 GHz. Trotter et al. (1998) interpret this variation as signifying an outer scale for the wavenumber spectrum of *anisotropically-scattering* density irregularities, $\ell_{\text{out}} \lesssim 10^{16}$ cm. This proposed outer scale is comparable to the thickness of the H II shell in this region (Rodríguez, Canto, & Moran 1988; Kahn & Breitschwerdt 1990). An alternate possibility is that the density irregularities scatter isotropically, but that the anisotropic images reflect density irregularities that are confined to the H II shell.

If the latter were the case, we would expect that the axial ratio would increase as a function

of decreasing frequency, opposite to what is observed. At lower frequencies, the size of the minor axis of the scattering diameter would be constrained by the width of the H II shell while the size of the major axis would be essentially unconstrained, unless the scattering is so intense that the size of the major axis is also limited by the scale of the H II shell. For NGC 6334B, the axial ratio appears to be constant with frequency or increasing with increasing frequency. The frequency behavior of the axial ratio indicates that any relevant length scales in the H II shell must be smaller than 10^{14} cm (the smallest length scale probed by the highest frequency observations) or larger than 10^{17} cm (the largest length scale probed by the lowest frequency observations).

5.3. Cygnus X-3

The compact source Cyg X-3 is heavily scattered ($0''.5$ at 1 GHz) and has an anisotropic image (axial ratio ≈ 1.2 and increasing with increasing frequency) whose position angle varies with frequency (Wilkinson, Narayan, & Spencer 1994; Molnar et al. 1995). The variation of position angle has been interpreted by Wilkinson et al. (1994) as due to a changing orientation of (anisotropic) diffracting irregularities on a length scale of order $\theta(D - D_s) \sim 0.01$ pc. In their picture, the image asymmetry is due to anisotropic diffracting irregularities, and the orientation change with frequency is attributed to the spatial variation of those irregularities.

An alternative explanation is that the diffracting irregularities are isotropic and that the image anisotropy reflects spatial variations of the strength of the diffracting irregularities on the scale $\theta(D - D_s)$. Molnar et al. (1995) have proposed that the H II region DR 11 is responsible for the bulk of the scattering along this line of sight. A key difficulty with this explanation is that the observed axial ratio increases with increasing frequency. This is inconsistent with the notion of scattering from a single filament but may be consistent with scattering from a group of filaments which are individually smaller than 10^{16} cm.

5.4. Sgr A* & Galactic-Center OH/IR Masers

Galactic center sources show large scattering diameters ($\sim 1''$ at 1 GHz) and significant image asymmetries that vary across the roughly $30'$ size of the scattering region (Lazio & Cordes 1998). The major axis of the image of Sgr A* shows a ν^{-2} frequency dependence from 1.4 to 22 GHz (Yusef-Zadeh et al. 1994; Lo et al. 1998), and the image itself displays no change in its major axis, axial ratio, or orientation on time scales as long as a decade (Lo et al. 1998; Marcaide et al. 1999).

Deviations from a ν^{-2} dependence for the major axis, minor axis, or both are claimed at a variety of frequencies from as low as 43 GHz (Lo et al. 1998) to as high as 215 GHz (Krichbaum et al. 1998). These deviations from the ν^{-2} dependence observed at lower frequencies are commonly interpreted as an effect of the intrinsic source diameter becoming important at the various frequencies.

The deviations could also be symptomatic of the size scale of the scattering medium. If this is the case, then the frequencies at which the breaks occur correspond to spatial scales $\ell \sim 5$ AU (for a break occurring at 43 GHz) to as small as 0.17 AU (at 215 GHz). These spatial scales are comparable to the outer scale inferred by Lazio & Cordes (1998), on the basis of a comparison of scattering strength and thermal free-free emission. However, the velocities in the Galactic center ($\sim 50 \text{ km s}^{-1}$) suggest that variations in the orientation of the image of Sgr A* should be seen on timescales of order $0.1 \text{ yr}(\ell/1 \text{ AU})(v/50 \text{ km s}^{-1})^{-1}$. As mentioned above, these are not seen. This implies either that all striations in the medium are oriented in the same direction or that the intrinsic source size is in fact important at high frequencies.

The lack of variations in the image orientation indicates that there are not likely to be striations or other structure in the scattering screen on scales smaller than about 1 AU. Variations do occur, though, on much larger scales, of order $15'$ corresponding to spatial scales of roughly 25 pc, the separations between Sgr A*, the various OH masers, and other scattered sources (Lazio et al. 1999). Effects from the spatially-limited scattering described in this paper are unlikely to be seen with the current census of Galactic center sources. The narrowband nature of OH masers means that the frequency dependence of their scattering diameters cannot be measured, and Sgr A* itself is obscured below 1 GHz due to free-free absorption by Sgr A. Detection of additional radio transients (e.g., Zhao et al. 1992) or radio pulsars (Cordes & Lazio 1997) may allow such effects to be detected at frequencies below 1 GHz.

5.5. Extreme Scattering Events

“Extreme scattering events” (ESE’s) are events identified in the light curves of several AGN’s (Fiedler et al. 1987; 1994) and two pulsars (Cognard et al. 1993; Maitia, Lestrade, & Cognard 1999). They are roughly consistent with *refractive* defocusing and caustic formation from discrete, small scale plasma structures (Fiedler et al. 1987; Romani et al. 1987; Clegg et al. 1998). However, alternative explanations invoke the outer ionized regions of predominantly neutral, primordial HI clouds (Walker & Wardle 1998) or distributed fluctuations much like those that account for the diffractive scintillations of pulsars (Fiedler et al. 1994). The fundamental difference between these models is the implied gas pressure. As discussed further below, a discrete structure is necessarily overpressured compared to the general ISM, so any such structures must exist either transiently or in regions of small volume filling factor that can support such pressure.

If ESEs result from discrete ionized structures, then effects described in this paper should be present in the scattered image and pulse shape (for pulsars). This notion is little explored because few ESEs have been identified and, given that most are seen from AGN’s, intrinsic source size effects can also diminish the appearance of diffraction effects. VLBI observations of the source 1741–038 undergoing an ESE have shown no indication of a truncated image (Lazio et al. 2000). However, those observations were at relatively high frequencies (≥ 1.7 GHz) and had limited dynamic range. Pulse timing observations of PSR B1937+21 (Cognard et al. 1997) show

no change in the pulse shape, though, again these observations were obtained at 1.4 GHz. Future observations of a source undergoing an ESE at lower frequencies (e.g., 0.33, 0.41, or 0.61 GHz) would place much more stringent constraints on the notion that ESEs arise from discrete ionized structures.

6. Future Observations

6.1. Application to Extragalactic Scattering

Scattering from extragalactic plasma can arise from the distributed intergalactic medium (IGM), most of which is expected to be ionized, from intervening Ly α clouds, and from intervening galaxies. Of greatest relevance to this paper are the last two cases and, of these, intervening galaxies are likely to be the more important because of their greater column densities. A face-on galaxy like the Milky way will scatter radiation from a background source into an apparent size of at least $\theta_d \sim 1 (\nu/0.33 \text{ GHz})^{-2.2}$ mas (Cordes & Lazio 1991; Taylor & Cordes 1993). Scattering by H II regions yields even larger angles, so some background sources, albeit at low-probability alignments, will display images that reflect the sizes of H II regions and, in some instances, spiral arms that contain them.

Scattering from an edge-on galaxy will be about 10^3 – 10^4 times larger, or $1''$ – $10''$ at 0.3 GHz.³ The lateral scale is $\theta_d D \sim 15$ – $150 \times D_{3000}$ kpc for $D = 3000 D_{3000}$ Mpc. Thus, near edge-on galaxies will produce scattered images that, in part, display the shapes of the galaxies. At even lower frequencies, scattering diameters from Ly α clouds and galaxies with significantly smaller scattering strength will produce similar effects. Imaging radio observations at ~ 0.1 GHz will thus probe intergalactic structures.

We defer to another paper a thorough discussion of intergalactic scattering, taking into account cosmological expansion and evolution. Scattering may be able to probe the intergalactic medium at redshifts near the reionization epoch.

6.2. Low-Frequency Galactic Observations

The (nominally) strong frequency dependence of interstellar scattering observables suggest that the anomalous scattering described here will most likely occur at low frequencies. High-resolution, low-frequency instruments such as the Giant Metrewave Radio Telescope (GMRT,

³ This large increase in the scattering diameter occurs because of the presence of enhanced scattering regions, such as those described in §5. In the Milky Way Galaxy, the approximate mean free path between enhanced scattering regions is 8 kpc (Taylor & Cordes 1993). A line of sight through the disk of a galaxy like the Milky Way is quite likely to encounter one or more enhanced scattering regions leading to the large increase cited.

Ananthkrishnan 1995) and the proposed Low Frequency Array (LOFAR, Kassim et al. 2000) and the low-frequency Square Kilometer Array (SKA, Butcher 2000) have or will have sub-arcminute resolution at frequencies below 150 MHz. Consequently, they may detect anomalous scattering along lines of sight less heavily scattered than those described in §5. Here we consider relevant lines of sight and frequencies for which anomalous scattering is a possibility.

The relevant length scale in regions of less intense scattering may be the outer scale of the density fluctuation spectrum ℓ_0 . (This may also be the relevant length scale in intense regions, though its value could be quite different and potentially much smaller.) Near the Sun (within ≈ 1 kpc), $l_0 \sim 1$ pc (Armstrong, Rickett, & Spangler 1995). It is unlikely that scattering diameters will probe this spatial scale (i.e., $\theta_d D \sim \ell_0$) unless $\nu < 10$ MHz. As the ionosphere becomes increasingly opaque at frequencies $\nu < 10$ MHz, ground-based interferometric arrays will likely not be affected by anomalous scattering in the solar neighborhood.

Toward the inner Galaxy, Galactic latitudes $|\ell| < 50^\circ$, stronger scattering than that in the solar neighborhood (but still weaker than the intense scattering described in §5) will obtain. In this case, observations at meter wavelengths may display anomalous scattering.

A competing effect for detecting anomalous scattering is free-free absorption. The density fluctuations responsible for interstellar scattering also contribute to free-free absorption. Sources seen along heavily scattered lines of sight at shorter wavelengths may be free-free absorbed at longer wavelengths. For instance, free-free absorption renders the Galactic center increasingly opaque for frequencies $\nu < 1$ GHz (Anantharamaiah et al. 1991).

7. Implications for the Interstellar Medium

As alluded to before, the existence of compact, turbulence-containing ionized structures is directly related to their longevity and rarity, or filling factor, in the Galaxy. Except for chance fluctuations from distributed turbulence, many observed phenomena suggest the existence of compact structures with densities that imply they are overpressured compared to most of the ISM. This is not overly surprising because the ISM is highly dynamic and is in pressure equilibrium only in some average sense. It is not known which kinds of locales (H II regions, supernova shocks, etc.) provide the largest scattering strengths. We suggest, simply, that the observable effects described in this paper might be used to better probe the physical sizes of regions that produce the largest levels of scattering.

Striations in interstellar gas densities on sub-parsec scales are most likely associated with magnetic fields. On diffraction scales $\lesssim 10^{11}$ cm, a compelling idea is that turbulence is essentially two dimensional and that irregularities are elongated along the field lines (Higdon 1984, 1986; Goldreich & Sridhar 1995). Larger scale filaments, such as those seen near the Galactic center perpendicular to the plane of the Galaxy (Yusef-Zadeh & Morris 1987), are also thought to be along the local field direction. If anisotropically diffracting irregularities are contained in screens

that are themselves elongated in the same direction, it may be difficult to separate (and thus identify) the two possible contributions to image elongation.

The frequency dependence of anomalous scattering may offer a means for identifying the cause of image elongation for a particular source if it is heavily scattered by a single (or few) filament(s) (cf. Figure 2 and §5). If the image elongation arises from anisotropic scattering by small-scale density irregularities, increased spatial resolution of the scattering material (e.g., by making observations at higher frequencies) may yield increased axial ratios as less spatial averaging is done over the small-scale irregularities (e.g., as argued by Wilkinson et al. 1994 for the image of Cyg X-3). This change in axial ratio is expected only if there are spatial variations of the orientation of scattering turbules. Conversely, if image elongation is produced by the boundaries of filaments, a different frequency dependence may be seen. A more complicated frequency dependence may result if the scattering results from a number of smaller filaments (e.g., Figure 6).

The wavenumber spectrum of electron density irregularities is often constrained by the scaling law of angular size and pulse broadening (and its reciprocal, the scintillation bandwidth) with frequency. For moderate scattering, where the dominant length scales are between the inner and outer scales, the pulse broadening time scales as ν^{-x} with $x = -2\beta/(\beta - 2)$, where β is the exponent of the three dimensional, isotropic wavenumber spectrum (CWB85; Rickett 1990). For a Kolmogorov spectrum, $\beta = 11/3$ and $x = 4.4$. If irregularities are isotropic, so that $\beta = 11/3$, but the medium is confined in the transverse direction, the actual value of x is lessened. The value of β inferred would be greater than $11/3$ in this instance. A similar trend occurs when angular broadening is used to infer β . It is not clear which, if any, of the published constraints on β are affected by the influence of scattering-region confinement. A detailed study of the wavenumber spectrum is deferred to another paper.

8. Summary

In this paper we have shown that radio scattering observables such as image shapes and pulse broadening functions can be strongly influenced by structure in the scattering medium on length scales substantially larger than those that cause the scattering. As such, careful multi-frequency observations can be used to constrain properties of the interstellar medium on scales that are typically ~ 1 – 10 AU. Intergalactic scattering has not been identified but is certainly expected from intervening spiral galaxies, probably expected for some Lyman- α clouds, and may occur from distributed ionized gas. For intergalactic scattering, relevant length scales can be comparable to the sizes of galaxies. A low-frequency VLBI survey of extragalactic sources may thus probe the level of scattering in other galaxies and in the general intergalactic medium. It is also expected that scattering of radiation from gamma-ray burst afterglows will be influenced in some cases by intervening ionized gas in the IGM as well as in the Milky Way’s ISM. These issues will be explored in separate articles.

We thank B. Rickett for helpful discussions. This work was supported by NSF Grant AST 9819931 to Cornell University. Basic research in radio astronomy at the NRL is supported by the Office of Naval Research.

REFERENCES

- Ananthakrishnan, S. 1995, JApAS, 16, 427
- Anantharamaiah, K. R., Pedlar, A., Ekers, R. D., & Goss, W. M. 1991, MNRAS, 249, 262
- Armstrong, J. W., Rickett, B. J., & Spangler, S. R. 1995, ApJ443, 209
- Backer, D. C. 2000, in Pulsar Astronomy—2000 and Beyond, IAU Colloquium 177, eds. M. Kramer, N. Wex, & R. Wielebinski (ASP: San Francisco) p. 499
- Backer, D. C., Wong, T., & Valanju, J. 2000, ApJ, 543, in press
- Bower, G. C. & Backer, D. C. 1998, ApJ, 496, L97
- Butcher, H. R. 2000, in Radio Telescopes, Proc. of SPIE Vol. 4015, ed. H. R. Butcher
- Clegg, A. W. and Fey, A. L. and Lazio, T. J. W., 1998, ApJ, 496, 253,
- Cognard, I. et al. 1993, Nature, 366, 320
- Cordes, J. M., Weisberg, J. M., & Boriakoff, V. 1985, ApJ, 288, 221. (CWB85)
- Cordes, J. M., & Lazio, T. J. 1991, ApJ, 376, 123.
- Cordes, J. M., Pidwerbetsky, A., & Lovelace, R. V. E. 1986, ApJ, 310, 737.
- Cordes, J. M. & Lazio, T. J. W. 1997, ApJ, 475, 557
- Cordes, J. M. & Rickett, B. J. 1998, ApJ, 507, 846
- Fey, A. L. and Spangler, S. R. and Cordes, J. M., 1991, ApJ, 372, 132
- Fiedler, R. L., Dennison, B., Johnston, K. J., & Hewish, A. 1987, Nature, 326, 675.
- Fiedler, R. L., Dennison, B., Johnston, K. J., Waltman, E. B., & Simon, R. S. 1994, ApJ, 430, 581.
- Goldreich, P. & Sridhar, S. 1995, ApJ, 438, 763
- Graham Smith, F. & Lyne, A. G. 2000, in Pulsar Astronomy—2000 and Beyond, IAU Colloquium 177, eds. M. Kramer, N. Wex, & R. Wielebinski (ASP: San Francisco) p. 503

- Hankins, T. H. 2000, in *Pulsar Astronomy—2000 and Beyond*, IAU Colloquium 177, eds. M. Kramer, N. Wex, & R. Wielebinski (ASP: San Francisco) p. 165
- Hankins, T. H. & Moffett, D. A. 1998, *BAAS*, 192, 570.
- Higdon, J. C. 1986, *ApJ*, 309, 342
- Higdon, J. C. 1984, *ApJ*, 285, 109
- Isaacman, R. & Rankin, J. M. 1977, *ApJ*, 214, 214.
- Kahn, F. & Breitschwerdt, D. 1990, *MNRAS*, 242, 209
- Kassim, N. E., Lazio, T. J. W., Erickson, W. C., Crane, P. C., Perley, R. A., & Hicks, B. 2000, in *Radio Telescopes*, Proc. of SPIE Vol. 4015, ed. H. R. Butcher, p. 328
- Krichbaum, T. P., Witzel, A. & Zensus, J. A. 1999, in *The Central Parsecs of the Galaxy*, ASP Conference Series 186, eds. Falcke, H. et al., 89
- Krichbaum, T. P., et al. 1998, *A&A*, 335, L106
- Lambert, H. C. & Rickett, B. J. 1999, *ApJ*, 517, 299
- Lazio, T.J.W. & Cordes, J. M. 1998, *ApJ*, 505, 715
- Lazio, T. J. W., Anantharamaiah, K. R., Goss, W. M., Kassim, N. E., & Cordes, J. M. 1999, *ApJ*, 515, 196
- Lazio, T. J. W., et al. 2000, *ApJ*, 534, 706
- Lo, K. Y., Shen, Z.-Q., Zhao, J.-H., & Ho, P. T. P. 1998, *ApJ*, 508, L61
- Lundgren, S. C., Cordes, J. M., Ulmer, M., Matz, S. M, Lomatch, S., Foster, R. S., & Hankins, T. H. 1995, *ApJ*, 453, 433.
- Lyne, A. G., & Thorne, D. J. 1975, *MNRAS*, 172, 97.
- Lyutikov, M. & Parkih, A. 2000, in *Pulsar Astronomy—2000 and Beyond*, ASP Conference Series, Vol. 202, eds. M. Kramer, N. Wex, & R. Wielebinski (San Francisco: ASP) p. 393
- Maitia, M., Lestrade, J.-F., & Cognard, I. 1999, *ApJ*, submitted
- Marcaide, J. M., Alberdi, A., Lara, L., Perez-Torres, M. A., & Diamond, P. J. 1999, *A&A*, 343, 801
- Molnar, L. A., Mutel, R. L., Reid, M. J., & Johnston, K. J 1995, *ApJ*, 438, 708.
- Rickett, B. J. 1990, *ARA&A*, 28, 561.

- Rodríguez, L. F., Canto, J., & Moran, J. M. 1988, *ApJ*, 333, 801
- Scheuer, P. A. G. 1968, *Nature*, 218, 920
- Sallmen, S., Backer, D. C., Hankins, T. H. & Lundgren, S. 1999, *ApJ*, 517, 460
- Taylor, J. H. & Cordes, J. M. 1993, *ApJ*, 411, 674 (TC93)
- Trotter, A.S., Moran, J. M. & Rodriguez, L. F. 1998, *ApJ*, 493, 666
- Vandenberg, N. R. 1976, *ApJ*, 209, 578
- Walker, M. & Wardle, M. 1998, *ApJ*, 498, 125
- Wilkinson, P. N., Narayan, R., & Spencer, R. E. 1994, *MNRAS*, 269, 67
- Williamson, I. P. 1972, *MNRAS*, 157, 55
- Williamson, I. P. 1973, *MNRAS*, 163, 345
- Williamson, I. P. 1975, *Proc. R. Soc. Lond. A.*, 342, 131
- Yusef-Zadeh, F. & Morris, M. 1987, *ApJ*, 320, 545
- Zhao, J., et al. 1992, *Science*, 255, 1538